ACS APPLIED MATERIALS & INTERFACES

www.acsami.org

Research Article

Acceleration of Oral Wound Healing under Diabetes Mellitus Conditions Using Bioadhesive Hydrogel

Jiwei Sun,[#] Tiantian Chen,[#] Baoying Zhao,[#] Wenjie Fan, Yufeng Shen, Haojie Wei, Man Zhang, Wenhao Zheng, Jinfeng Peng, Jinyu Wang, Yifan Wang, Lihong Fan, Yingying Chu,[*] Lili Chen,[*] and Cheng Yang[*]

Cite This: *ACS Appl. Mater. Interfaces* 2023, 15, 416−431

Read Online

ACCESS | Metrics & More | Article Recommendations | Supporting Information

ABSTRACT: Oral wounds under diabetic conditions display a significant delay during the healing process, mainly due to oxidative stress-induced inflammatory status and abnormal immune responses. Besides, the wet and complicated dynamic environment of the oral cavity impedes stable treatment of oral wounds. To overcome these, a biomimetic hydrogel adhesive was innovatively developed based on a mussel-inspired multifunctional structure. The adhesive displays efficient adhesion and mechanical harmony on the oral mucosa through enhanced bonding in an acidic proinflammatory environment. The bioadhesive hydrogel exhibits excellent antioxidative properties by mimicking antioxidative enzymatic activities to reverse reactive oxygen species (ROS)-mediated immune disorders. Experiments on oral wounds of diabetic rats showed that this hydrogel adhesive could effectively protect against mucosal wounds and obviously shorten the inflammatory phase, thus promoting the wound-healing process. Therefore, this study offers a promising therapeutic choice with the potential to advance the clinical treatment of diabetic oral wounds.

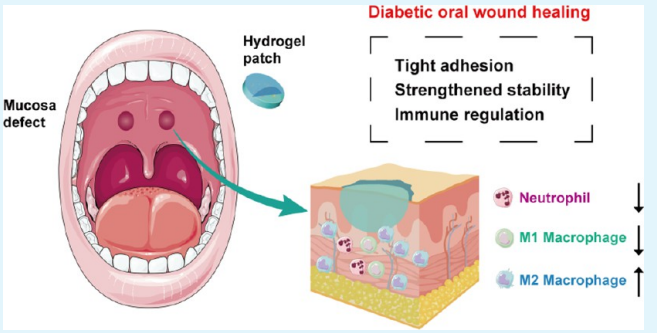

KEYWORDS: *diabetic oral wounds, wet adhesion, antioxidative stress, immunomodulation, hydrogel patch*

INTRODUCTION

More than 30% of adults suffer from oral wounds caused by ulceration, trauma, and dentofacial surgery, which seriously affect the life quality of patients.[1−3] Normally, mucosal tissues in the oral cavity would activate an expedited healing process including re-epithelialization, new connective tissue formation, and histological structure rearrangement[4,5] upon being injured. Unlike skin tissues, the oral mucosa, which is classified as a nonkeratinized tissue, exhibits less proinflammatory reaction during the healing process, thus shortening its self-repairing process.[6] However, some systemic diseases, especially diabetes, could significantly slow down the healing process of oral mucosal wounds due to very high glucose levels, high levels of advanced glycation end products (AGEs), increased formation of reactive oxygen species (ROS), and a subsequently strengthened inflammatory phase.[7,8] AGEs can interact with AGE receptors (RAGE) expressed on multiple types of cells, resulting in the activation of inflammatory signaling pathways, NF-κB for example, and subsequent production of proinflammatory cytokines in the extracellular microenvironment.[9] In addition, hyperglycemia-induced mitochondrial ROS production would stimulate AGEs and the classic protein kinase C (PKC) pathway, thus leading to pathological changes in inflammatory gene expressions, including IL-1β and IL-18.[10]

The most predominant characteristics in this abnormal inflammation status are greater numbers of neutrophils and reduced conversion of the M1 to M2 macrophage phenotype.[11−13] This might be derived from abnormalities in inherent mesenchymal stem cells under diabetic conditions, impairing the immunomodulatory functions, which would contribute to the enhanced production of proinflammatory cytokines and NLRP3 inflammasome activation.[14] Current medical interventions aimed at this situation include collagen-derived wound dressing,[15] local glycemic control,[16] cellulose sponges,[17] and exogenous application of bioactive factors such as epidermal growth factor (EGF) and vascular endothelial growth factor (VEGF).[18,19] However, these clinical treatments are either expensive for popularization or unable to realize optimal effects on the regulation of the immune status. The antioxidant function has recently been considered as an ideal

Received: September 27, 2022
Accepted: December 6, 2022
Published: December 23, 2022

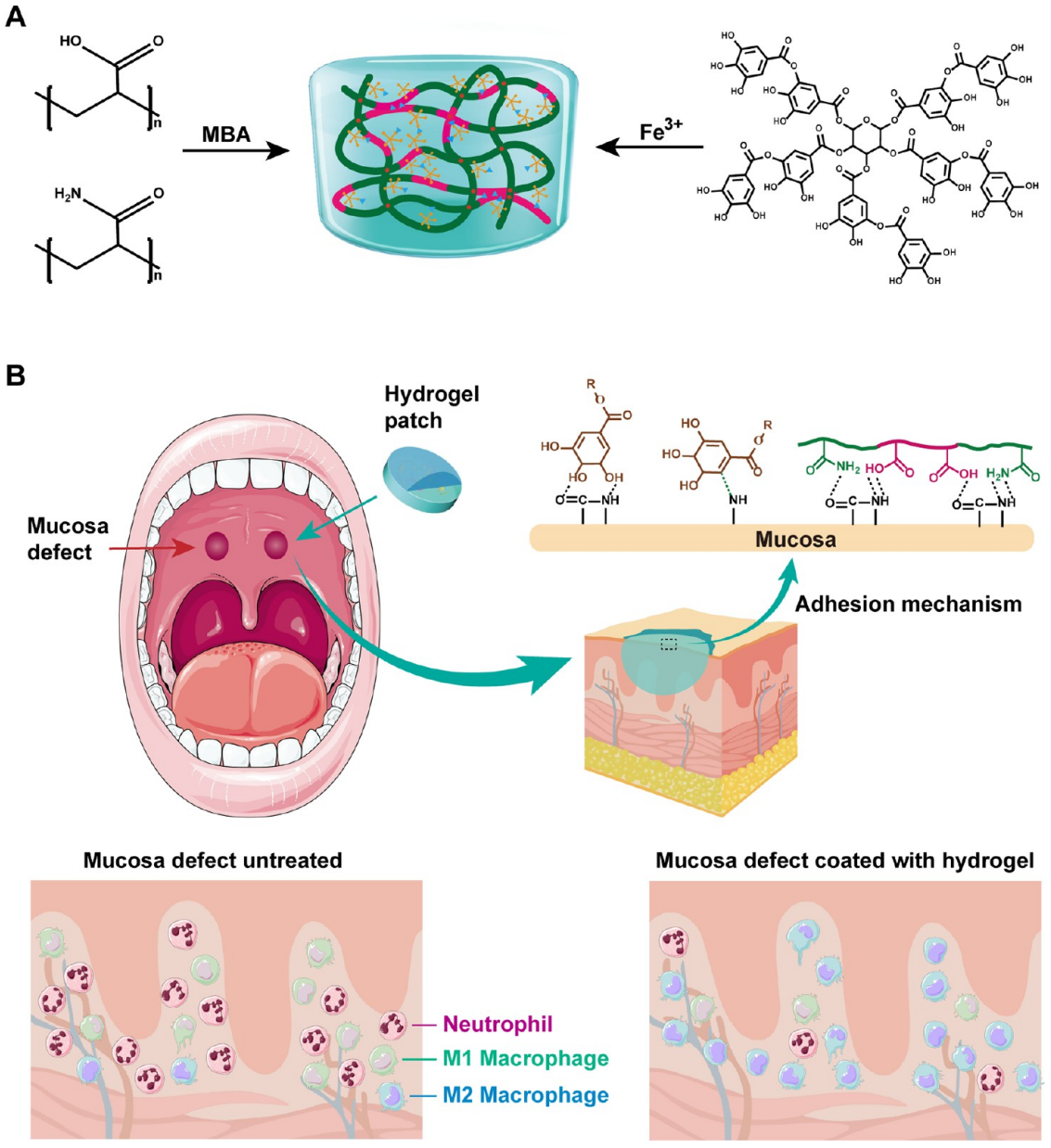

Figure 1. Formation and adhesion mechanism of an Fe-TA@P(AM-AA) hydrogel and its application. (A) Schematic diagram of the formation of the adhesive gel. Monomers of acrylamide and acrylic acid were first linked by radical polymerization to form a long-chain backbone network. The double-crosslinked system was finally constructed by the electrostatic interaction and hydrogen bonding between the Fe-TA complex and the backbone network. The special tissue adhesive potential was mainly attributed to the dynamic bonding between molecular groups from the tissue surface and composite gel shown above. (B) Application of Fe-TA@P(AM-AA) for the promotion of oral mucosal wound healing in diabetes by tight adherence on host oral tissues, resistance to the oral microenvironment, prevention of bacterial invasion, antioxidative activity, and improvement of the proinflammatory status. The combination of adhesion, fatigue resistance, and biological function make the Fe-TA@P(AM-AA) gel extremely superior.

property in the care of diabetic wounds, as an overdose of ROS significantly intensifies local inflammation.[20] Thus, oral dressings accompanied by excellent ROS scavenging potential might be highly desirable in oral wounds under diabetic conditions.

On the other hand, the wet, dynamic, and unstable environment in the oral cavity consisting of a continuous flush of saliva and bathing of exogenous food and drinks makes the persistent attachment and retention of the wound dressing more difficult.[21] Nevertheless, current agents applied in oral wound protection, including powders and films, might face the challenge of being washed away or degraded, thus failing to play a consistent and adequate role in the promotion of wound healing.[22] Application of current adhesives, including bioglues and resin-based dressings, are limited in oral wounds due to their toxicity, instability, weak bonding, and inconvenience in operation.[23−25] These deficiencies restrained the above adhesives in clinical application.

In this study, we developed a mussel-inspired multifunctional hydrogel adhesive that combined pH-sensitive noncovalent anchoring on wet tissues, strengthened mechanical properties, enhanced structural conformance, and the biomimetic role of antioxidase activities, thus meeting the specific requirements for the effective protection and healing of oral

https://doi.org/10.1021/acsami.2c17424
ACS Appl. Mater. Interfaces 2023, 15, 416−431

wounds under diabetic conditions. We designed a Fe^{3+}-tannin (Fe-TA) complex-modified P(AM-AA) hydrogel (Fe-TA@P(AM-AA)) that can simultaneously induce tissue adhesion and structure strengthening. The polyphenol groups were anchored to amino groups on the tissue rapidly via hydrogen bonding, achieving a stable attachment and protection for oral wounds. Simultaneously, Fe^{3+} derived from complexes coordinated with functional groups in poly(acrylic acid) (PAA) chains to achieve strengthened mechanical properties, thus avoiding unexpected destructions in the dynamic oral environment. More importantly, the hydrogel exhibited a stronger adhesion in response to the lower pH level in the prolonged inflammatory status under diabetic conditions. This could be explained by the increased content of −COOH at inflammatory wounds, resulting in enhanced hydrogen bonding between carboxyl groups and H^+ as well as strengthened electrostatic interactions between −COOH in the system and $-NH_2$ on the tissue surface. In addition, the Fe-TA complex could biomimetically exert enzymatic activities on diabetes-mediated local oxidative stress through the release of tannin with polyphenol groups to interact with environmental ROS products by a redox reaction, leading to a predominant reversal of excessive neutrophil infiltration and imbalance between M1 and M2 macrophages.[26] The application of our adhesive on oral injuries of diabetic rats indicated that the hydrogel successfully protected the defect regions and converted diabetes-induced local inflammation, thus promoting the wound-healing process (Figure 1). The superior performance of our gel exhibited its potential value for clinical application in dressings for oral mucosal defects in diabetic patients, casting light on the method of care and treatment specifically aimed at relieving the chronic pain of diabetic oral wounds.

MATERIALS AND METHODS

Materials. The reagents acrylamide monomer (AAM) and *N*,*N*′-methylenebisacrylamide (MBA) were purchased from Aladdin Reagent Co. (Shanghai). Tannic acid (TA) and ferric chloride hexahydrate ($FeCl_3 \cdot 6H_2O$) were purchased from Maclean's Reagent Co. Acrylic acid (AA) and ammonium persulfate (APS) were purchased from Sinopharm Chemical Reagent Co. All chemicals were analytical grade reagents and used without further treatment.

Methods. *Preparation of the Fe-TA@P(AM-AA) Hydrogel.* The multifunctional dual-crosslinked hydrogels based on acrylic acid and acrylamide were prepared via a one-step synthesis. First, PAA (0.5 g) was dissolved in 8 mL of MBA (20 mg) solution, followed by the addition of PAM (1.5 g) into the mixed solution, and stirred for 5 min. Afterward, 2 mL of the Fe-TA complex solution composed of 1 mL of TA solution (20 mg/mL) and 1 mL of Fe^{3+} solution with various concentrations (0, 5, 10, and 20 mg/mL) was dispersed into the above solution, respectively. Then, following further stirring, the homogeneous solution was vacuumed for 5 min to eliminate bubbles. Finally, APS (0.03 g) was added to the solution to initiate the reaction with the assistance of MBA as the crosslinking agent and Fe-TA as the metal catalyst. The samples were labeled according to the percentage of Fe^{3+} content.

Characterization of the Fe-TA@P(AM-AA) Hydrogel. Ultraviolet−Visible (UV−Vis) Absorption Spectroscopy. The successful preparation of Fe-TA complexes was confirmed by UV−vis analysis. Specifically, Fe-TA complex solutions containing different Fe^{3+} concentrations were diluted to 1 mg/mL, respectively, and the spectra of the samples were recorded on a UV−Vis spectrometer (Lambda 750 S, PerkinElmer) in the range of 200−800 nm.

Fourier Transform Infrared (FT-IR) Absorption Spectroscopy. To study the gelation mechanism of hydrogels, certain amounts of PAM, TA, and the Fe-TA@P(AM-AA) hydrogel solid were prepared, respectively. The spectra of the samples were determined by Fourier transform infrared (FT-IR) spectroscopy (Nicolet 5700 FT-IR Spectrometer, Thermo Fisher Scientific) using the pressed slice method in the wavelength range of 4000−400 cm^{-1}.

Raman Spectroscopy. Raman spectra of PAM, TA, and Fe-TA@P(AM-AA) hydrogels were measured via a Raman microscope (Thermo Scientific DXR) with a 785 nm laser light as the excitation source, and the laser power was set at 25 mW.

Scanning Electron Microscopy (SEM) Analysis. To assess the microstructure of the prepared hydrogels, each group of hydrogels was prepared to 300 μL volume. The samples were placed in a refrigerator at −80 °C for 12 h and then freeze-dried for 48 h. The freeze-dried samples were placed in liquid nitrogen for brittle fracture, and then the cross-section was coated via a gold spray. The internal microstructure of the hydrogel was observed under a scanning electron microscope (SEM, Gemini 6000, ZEISS, Germany).

Swelling Behavior. To characterize the swelling behavior, the prepared hydrogels with different contents of Fe^{3+} were soaked in phosphate-buffered saline (PBS) (pH = 7.4) for 48 h at 37 °C. At each predesignated time interval, the hydrogels were collected and weighted (W_1). The weight of the initial sample was determined (W_0), which allowed us to calculate the swelling ratio as follows

$$\text{swelling ratio}\ (\%) = W_1/W_0 \times 100\%$$

Excellent Adhesive Performance of Fe-TA@P(AM-AA) Gels. Lap Shear Tests. To evaluate the bioadhesive performance of the hydrogels, we then conducted lap shear tests to measure the adhesive strength of various hydrogels. The hydrogels were applied to the surface of fresh porcine skin with a bonded area of 10 mm × 10 mm. The samples were pulled to failure at a crosshead speed of 5 mm/min until the samples separated, using a universal testing machine (Instron 5567). To characterize the wet adhesion capacity of the hydrogel, two pieces of porcine skin samples were stuck together by the hydrogel in pure water for 12 h, and the corresponding adhesive properties were investigated. The adhesion strength was calculated by the maximum load divided by the initial bonded area. Three samples were tested to determine the adhesive strength of each group (n = 3).

SEM Analysis. To evaluate the integration of the tissue and the hydrogel, the hydrogel was applied in situ on fresh rat mucosal tissues. The samples were lyophilized, dehydrated, and observed under a scanning electron microscope with gold−palladium coating.

Simulated Saliva Environment Test. We established a testing model to characterize the adhesion capacity of the hydrogel in the wet oral environment. Porcine skin samples were immersed in artificial saliva with different pH values (3.0, 5.5, 6.8, and 8.0) before adhesion. The subcutaneous tissue side of the skin strips was coated with the gels, and the adhesion capacity was tested by a universal testing machine.

Mechanical Properties of Fe-TA@P(AM-AA) Hydrogels. Mechanical Property Tests. Mechanical tests were carried out on the as-prepared hydrogels using a universal mechanical testing machine. The samples were prepared on dumbbell-shaped molds and pulled to failure at a rate of 10 mm/min. For compression tests, the hydrogel samples were prepared in cylindrical-shaped tetrafluoroethylene molds with a diameter of 10 mm and a height of 10 mm. Cyclic compression tests were conducted three times at strains of 30, 50, and 70%. The testing speed was set at 5 mm/min.

Rheological Tests. Rheological measurements were performed on a Discovery HR-2 rheometer (TA Instruments) using a flat plate (40 mm diameter). The storage modulus (G') and loss modulus (G'') of the hydrogels were determined in the oscillation frequency mode under 10% constant strain, with ω varied from 1 to 100 rad/s at 37 °C. The critical strain point of the hydrogel was detected by a strain amplitude sweep test from 10 to 1000% strain at a fixed oscillation frequency of 10 rad/s. The alternate step strain sweep test was carried out at 37 °C to test the self-healing properties of the hydrogel. The strain was periodically switched from a small strain (10%) to a subsequent large strain (1000%) with 100 s for every strain interval. The self-healing behavior was also quantitatively evaluated through a tensile−heal−tensile test. The hydrogel was cut in the middle, and

https://doi.org/10.1021/acsami.2c17424
ACS Appl. Mater. Interfaces 2023, 15, 416−431

then, the two separate parts were brought in contact with each other and self-healed, and the entire process was observed for less than 5 min.

Cell Culture. Oral epithelial cell lines and THP-1 cells were obtained from the American Type Culture Collection (ATCC). Oral epithelial cells were cultured in Dulbecco's modified Eagle's medium (DMEM)/high glucose (Cytiva) supplemented with 10% fetal bovine serum (FBS), while THP-1 cells were cultured in RMPI Medium Modified (Cytiva) containing 10% FBS. All cells were maintained in a humidified cell culture incubator with 5% CO_2 at 37 °C.

Indirect Coculture. Glucose anhydrose (Macklin, G6172) was dissolved in the culture medium (900 g/L). Subsequently, the solution was passed through a 0.22 μm filter (Biosharp) and mixed with RMPI Medium Modified (Cytiva) at a ratio of 1:1 to generate a high-glucose medium at a final concentration of 450 g/L to simulate diabetic conditions in vitro. Composite hydrogel samples at different Fe-TA concentrations (P(AM-AA), FeTA-10, and FeTA-20) were incubated in the culture medium at 37 °C for 24 h after 1 h irradiation under ultraviolet light for sterilization. Then, the supernatants were extracted and filtered with a 0.22 μm filter and then mixed with the high-glucose medium (450 g/L) described previously at a ratio of 1:10. Oral epithelial cells were cultured in DMEM/high glucose (Cytiva). THP-1 cells were cultured in Roswell Park Memorial Institute (RPMI) medium modified (Cytiva) containing PMA at a concentration of 100 ng/mL. After 24 h, the culture media of oral epithelial cells and THP-1 cells were removed and replaced with the above mixture (high-glucose medium and composite hydrogel supernatants). Cells cocultured with P(AM-AA) extract were taken as the control group.

Cellular Protein Extraction. Macrophages cocultured with different hydrogel extracts for 48 h were lysed with radioimmunoprecipitation assay (RIPA) lysis buffer (Beyotime, P0013B) supplemented with protease inhibitors (Invivogen) at a ratio of 100:1 on ice. The liquids were centrifuged at 12,000 rpm for 20 min. The supernatants were gathered to obtain the total protein, and the protein concentration was quantitated using a BCA Protein Assay Kit (Beyotime, P0012).

Intracellular Antioxidative Properties. Reactive Oxygen Species Assay. A reactive oxygen species assay kit (Beyotime, S0033S) was employed to measure the total intracellular reactive oxygen species (ROS) of macrophages cocultured with different hydrogel extracts for 48 h following the manufacturer's protocol. In brief, the cells were incubated with a 1:1000 v/v mixture of dichlorodihydrofluorescein diacetate (DCFH-DA) and RPMI 1640 medium in a cell incubator at 37 °C for 20 min. After washing three times with PBS solutions, images were obtained by a fluorescence microscope at 488 nm excitation wavelength and 525 nm emission wavelength.

Superoxide Dismutase (SOD) Assay. The intracellular superoxide dismutase (SOD) activity was detected with the Cu/Zn-SOD and Mn-SOD Assay Kit with WST-8 (Beyotime, S0103) according to the manufacturer's protocol. In brief, proteins of macrophages were extracted as described previously. Before the experiment, the WST-8/enzyme working solution and reaction start-up solution were prepared. When everything was ready, the samples, SOD assay buffer, WST-8/enzyme working solution, and reaction start-up solution were added into 96-well plates, respectively, according to the instructions and incubated at 37 °C for 30 min. Finally, the absorbance was measured at 450 nm, and SOD activities were calculated.

Catalase Assay. Similarly, the protein of macrophages was extracted, and concentrations of samples were measured. The intracellular catalase activity was determined using a Catalase Assay Kit (Beyotime, S0051), following the instructions of the manufacturer. In brief, after obtaining the standard curve, samples were determined using the assay kit, and the OD value at 520 nm was measured after incubation at 25 °C for 20 min. Subsequently, the catalase activities of samples were calculated using the OD values and protein concentrations according to the standard curve.

2,2-Di(4-tert-octylphenyl)-1-picrylhydrazyl (DPPH) Free Radical Scavenging Test. The free radical scavenging capability of different composite hydrogels in vitro was measured by the DPPH method. The DPPH solution (0.1 mmol/L, in anhydrous ethanol) was prepared in advance. Composite hydrogels (0.1 g) were incubated with DPPH solution (1 mL) for 30 min in the dark at room temperature. The DPPH solution (1 mL) group and anhydrous ethanol (1 mL) group were incubated for 30 min at the same time to serve as the control group. Subsequently, the absorbance at 520 nm was measured, and the free radical scavenging capability was calculated.

Total RNA Extraction. Cells were seeded into six-well plates and incubated with different composite hydrogels for 48 h. Then, 1 mL of TRIzol reagent (Takara) was added to each well for cell lysis, followed by incubation for 5 min at room temperature to dissociate the nucleoprotein complexes. The cell lysates were transferred to an Eppendorf microcentrifuge tube and mixed with 0.2 mL of chloroform for homogenization. The samples were centrifuged at 12,000 rpm for 15 min at 4 °C after incubation for 3 min at room temperature. The upper aqueous phase was transferred carefully into a fresh tube. An equal volume of isopropanol was added to the fresh tube to precipitate the RNA. The samples were incubated at room temperature for 10 min and centrifuged at 12,000 rpm for 10 min at 4 °C. The supernatants were removed carefully, and the RNA pellets were washed with 75% ethanol. The samples were centrifuged at 7500 rpm for 5 min at 4 °C, followed by the removal of leftover ethanol. The RNA pellets were dried for 10 min at room temperature and dissolved in 20 μL of RNase-free water.

Real-Time Quantitative Polymerase Chain Reaction (PCR). Reverse transcription was performed using a HiScript III RT SuperMix for qPCR (+gDNA wiper) (Vazyme) to generate cDNA. Then, quantitative real-time PCR was performed using a ChamQ SYBR qPCR Master Mix (Vazyme) on a real-time PCR system (ABI 7300, Applied Biosystems). Relative mRNA expression levels were normalized against the expression level of h-GAPDH by the $2^{-\Delta\Delta Ct}$ method. The primers used in this study are listed in Table S1.

Immunofluorescence Staining. Cells were seeded at a density of 5 × 10^4 cells per well in 12-well plates with sterile glass coverslips, and the cell confluency was about 30−50%. After incubation with composite hydrogels as described previously, cells were washed with PBS three times and fixed with 4% paraformaldehyde (PFA) for 20 min. Subsequently, they were blocked with 5% bovine serum albumin (BSA) for 1 h, followed by incubation with primary antibodies anti-CD86 (ABclonal, A1199, 1:200) and anti-CD206 (Proteintech, 60143-1-Ig, 1:200), respectively, at 4 °C overnight. The cells were then incubated with CoraLite488-conjugated secondary antibody (Proteintech, 1:200) and cy3-conjugated secondary antibody (Proteintech, 1:200), respectively, for 1 h in a humidified chamber at room temperature. The cell nuclei were counterstained with 4′,6-diamidino-2-phenylindole (DAPI) for 5 min. Images were obtained by a confocal laser scanning microscope (Nikon A1-Si) and analyzed by ImageJ (NIH).

Biocompatibility Evaluation. Cell Counting Kit-8 (CCK-8) Assay. The biocompatibility of composite hydrogels was determined on oral epithelial cells using Cell Counting Kit-8 (CCK-8) (Beyotime, C0038) according to the manufacturer's instructions. In brief, cells were seeded into 96-well plates and cocultured with different hydrogel extracts for 1, 3, and 5 days, respectively, to perform the CCK-8 assay. The culture medium and CCK-8 reagents were added to each well at a ratio of 9:1, followed by incubation at 37 °C for 1 h. Subsequently, the optical density was measured at 450 nm wavelength.

Live/Dead Cell Staining. Cell cytotoxicity of the gel was assessed with oral epithelial cells cocultured with different hydrogel extracts for 48 h using a Calcein AM/PI Double Stain Kit (MKBio, Shanghai, MX3012) following the manufacturer's protocols. After the preparation of the assay buffer and stain buffer, cells were incubated with the stain buffer at 37 °C for 15 min. Fluorescent images were captured on a confocal microscope (Nikon A1-Si).

Cell Skeleton Staining. To observe the cell adhesive behavior of macrophages after coculturing for 48 h with different hydrogel extracts, F-actin staining was then performed as described below. Cells were first fixed with 4% PFA for 20 min and permeated with 0.1% Triton X-100 for 20 min. After that, they were blocked with 5% BSA for 1 h, followed by incubation with TRITC-phalloidin (Solarbio) for

https://doi.org/10.1021/acsami.2c17424
ACS Appl. Mater. Interfaces 2023, 15, 416−431

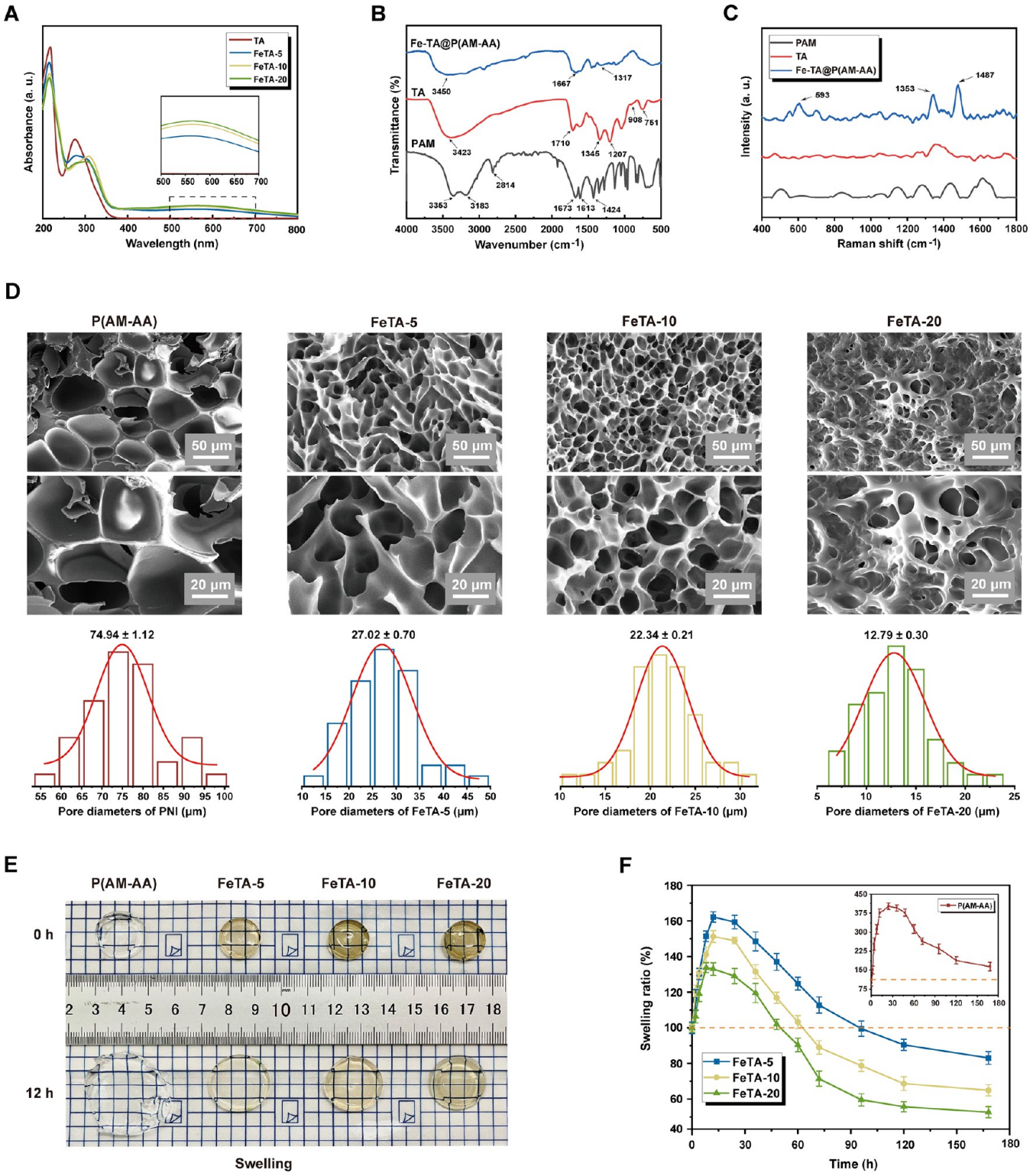

Figure 2. Structural characterization of the Fe-TA@P(AM-AA) hydrogel. (A) UV−vis absorption spectra of the TA/Fe complex solution with different Fe^{3+} concentrations (0, 5, 10, and 20 mg/mL). (B) FT-IR spectra of PAM, TA, and Fe-TA@P(AM-AA) hydrogels. (C) Raman spectra of PAM, TA, and Fe-TA@P(AM-AA) hydrogels. (D) SEM images and diameter analysis of Fe-TA@P(AM-AA) hydrogels. (E, F) Swelling properties of the Fe-TA@P(AM-AA) hydrogels with different Fe^{3+} concentrations in phosphate-buffered saline, pH = 7.4.

30 min to label F-actin. Nuclear counterstaining was performed using DAPI for 5 min. Images were acquired using a fluorescence microscope.

Western Blot Analysis. Protein lysates were mixed with 5× sodium dodecyl sulfate (SDS) loading buffer (Beyotime, P0286) at a ratio of 1:4 and heated for 5 min at 95 °C for protein denaturation. Samples (30 μg) were separated by 10% sodium dodecyl sulfate polyacrylamide gel electrophoresis (SDS-PAGE) and transferred to 0.45 μm poly(vinylidene fluoride) (PVDF) membranes. The membranes were blocked with 5% skimmed powdered milk for 1 h at room temperature, followed by incubation with primary antibodies at 4 °C overnight. Then, the membranes were incubated with

https://doi.org/10.1021/acsami.2c17424
ACS Appl. Mater. Interfaces 2023, 15, 416−431

horseradish peroxidase (HRP)-conjugated secondary antibodies (Proteintech) for 1 h at room temperature. Autoradiograms were obtained with an enhanced chemiluminescence detection system and recorded using an X-ray film. The gray value of each Western blot band was measured by ImageJ Software. The primary antibodies are anti-GAPDH (Proteintech, 10494-1-AP) and anti-CD206 (Proteintech, 18704-1-AP).

Cell Apoptosis Assay. Cell apoptosis in epithelial cells incubated with different composite hydrogel extracts was detected by flow cytometry using an Annexin V-FITC/PI-PE Apoptosis Detection Kit (Vazyme, A211-02) following the manufacturer's protocol. In brief, $(1-5) \times 10^5$ cells were collected and centrifuged for 5 min at 1800 rpm, followed by washing with cold PBS twice. Cells were resuspended with 100 μL of 1× binding buffer and stained with 5 μL of Annexin V-FITC and 5 μL of PI Staining Solution for 10 min at room temperature in the dark. Apoptosis in cells was analyzed by a BD FACS Canto II Flow Cytometer immediately.

Flow Cytometry. M2 polarized macrophages were quantified by flow cytometry using the APC Anti-Mouse CD206 Antibody (Elabscience, E-AB-F1135E). In brief, 1×10^6 cells were collected and washed with cold PBS, after which the cells were fixed with 4% paraformaldehyde for 20 min, followed by incubation with 1% BSA for 1 h at room temperature. Then, 5 μL of flow cytometry antibody in 100 μL of PBS was added to each sample for 30 min incubation in the dark. Subsequently, the samples were washed with PBS and analyzed by a BD FACS Canto II Flow Cytometer.

Diabetic Rat Model. All animal experiments were conducted in accordance with the current ethical guidelines of the Animal Care and Use Committee of Tongji Medical College, Huazhong University of Science and Technology.

In this study, adult Sprague Dawley (SD) rats (male, 6−8 weeks) purchased from Beijing HFK Bioscience Co. Ltd. (Beijing, China) were allowed to adapt to our laboratory environment for 1 week. Type 2 diabetic models were established based on acknowledged protocols. In brief, streptozotocin (STZ, 500 mg, Sigma, S0130) was dissolved in sodium citrate buffer (pH 4.5) to obtain a 1% STZ solution. After 4−6 weeks of feeding a high-fat diet, SD rats fasted for 12 h were then intraperitoneally injected with a low-dose STZ solution (30 mg/kg) to generate a model of type 2 diabetes. The rats with fasting blood glucose levels above 12 mmol/L for 14 days after STZ injection were diagnosed with diabetes and ready for the establishment of the oral wound model described in the following section.

Rat Oral Wound Model and Treatment. Sixty diabetic SD rats were used in this study. The rats were randomly divided into four groups: (1) 15 rats killed at 1 day after treatment; (2) 15 rats killed at 3 days after treatment; (3) 15 rats killed at 5 days after treatment; (2) 15 rats killed at 7 days after treatment. After the diabetic rats were anesthetized, the same size defects to the epithelium and lamina propria on both sides of the palatal mucosa were created using a 1.2 mm diameter ball drill. After hemostasis, FeTA-10 was coated on the palatal mucosal defect on the right side, while the defect on the left side was not coated with anything to serve as the control. Rats were killed at 1, 3, 5, and 7 days after treatment, and wound areas were measured and calculated using image analysis software.

Bacterial Detection and Analysis. At 12, 24, and 48 h after treatment, the bacteria on the palatal mucosa defects of both the treated group and the control group were obtained by small sterile cotton swabs after successful anesthesia. The bacteria were cultured in Luria−Bertani (LB) medium at 37 °C for 24 h, and the number of bacteria in each group was assessed by measuring the absorbance of the bacterial liquid at 600 nm.

Histological Section Preparation. Cryosections. Immediately after coating the mucosal defects with gels, the rats were sacrificed, and the tissues of wound areas were prepared to observe the adhesive performance of the gel in the oral mucosa tissue. In brief, the surgical specimens were covered with the embedding medium and frozen rapidly to about −20 to −30 °C. Subsequently, the samples were cut into 6 μm thick serial slices and placed on glass slides.

Paraffin Sections. Rat palatal mucosa defect specimens were collected and fixed with 4% PFA at 12, 24, and 48 h after the treatment, respectively. In brief, the samples were dehydrated with a series of progressively more concentrated ethanol (70, 80, 90, 95, and 100%). Subsequently, xylene was added to remove the ethanol. After embedding in paraffin, the specimens were cut into 5 μm thick sections.

Hematoxylin−Eosin (H&E) Staining. For the morphological observation of the palatal mucosa sections processed in both ways, hematoxylin−eosin staining (H&E) was conducted following routine procedures. In brief, after deparaffinization and rehydration, histological sections were incubated with hematoxylin for 5 min to stain the cell nuclei, followed by incubation with acidic ethanol and aqua ammonia. Subsequently, specimen sections were rinsed in distilled water and stained with eosin for 3 min, followed by dehydration and clearing with xylene. Histological characteristics of the sections were observed under an optical microscope.

Immunofluorescence on Histological Sections. Rat paraffin-embedded palatal mucosa tissue sections were blocked with 5% bovine serum albumin (BSA) at room temperature for 1 h. Subsequently, the histological sections were incubated with the following primary antibodies, respectively, at 4 °C overnight: anti-CD16 (Proteintech, 16559-1-AP), anti-CD86 (ABclonal, A1199), anti-CD206 (Proteintech, 60143-1-Ig), anti-CD31 (Abcam, ab28364), and anti-Ki67 (Abcam, ab1558). After washing with PBS three times, the slides were incubated with the CoraLite488-conjugated secondary antibody or cy3-conjugated secondary antibody in the dark. The nuclei were counterstained with DAPI, and images were captured with a confocal microscope (Nikon A1-Si).

Statistical Analysis. All quantitative data were analyzed using GraphPad Prism 8 statistical software and presented as means ± standard deviation (SD). Significant differences were determined by an unpaired *t*-test for comparison between two groups and one-way analysis of variance (ANOVA) followed by Dunnett's multiple comparison test for multiple comparisons. P values <0.05 were considered to be statistically significant. Symbols *, **, ***, and **** represent $P < 0.05$, $P < 0.01$, $P < 0.001$, and $P < 0.0001$, respectively.

RESULTS AND DISCUSSION

Synthesis and Characterization of Fe-TA@P(AM-AA) Gels. Based on our design, Fe-TA complexes containing different concentrations of Fe^{3+} were prepared via a one-step physical crosslinking reaction, which was then utilized to catalyze free radical copolymerization of acrylamide and acrylic acid monomers with the assistance of APS as the radical initiator and MBA as the crosslinking agent to yield Fe-TA@P(AM-AA) hydrogels. Specifically, the successful preparation of the Fe-TA complex was verified by UV−vis analysis as the significant absorption peak around 570 nm was attributed to the coordination bond in Fe-TA chelates (Figure 2A). Afterward, Fourier transform infrared (FT-IR) spectroscopy was employed to prove the successful manufacture of Fe-TA@P(AM-AA) hydrogels. Specifically, the shift of the −OH stretching vibration peak from 3423 to 3450 cm^{-1} in the spectra of Fe-TA@P(AM-AA) hydrogels when compared with that of TA could be attributed to the formation of hydrogen bonds as well as the electrostatic interaction between Fe-TA and PAA. In addition, the adsorption band of C═O at 1710 cm^{-1} in TA and 1673 cm^{-1} in pure PAM hydrogel shifted to 1667 cm^{-1} in Fe-TA@P(AM-AA), further confirming the formation of hydrogen bonds during the crosslinking process (Figure 2B). In addition, the Raman spectral analysis exhibited obviously new peaks at 593, 1353, and 1487 cm^{-1} due to the vibration of the Fe−O bond between Fe^{3+} and the −OH of TA, indicating the formation of coordinated Fe-TA complexes within the network of the Fe-TA@P(AM-AA) hydrogel

https://doi.org/10.1021/acsami.2c17424
ACS Appl. Mater. Interfaces 2023, 15, 416−431

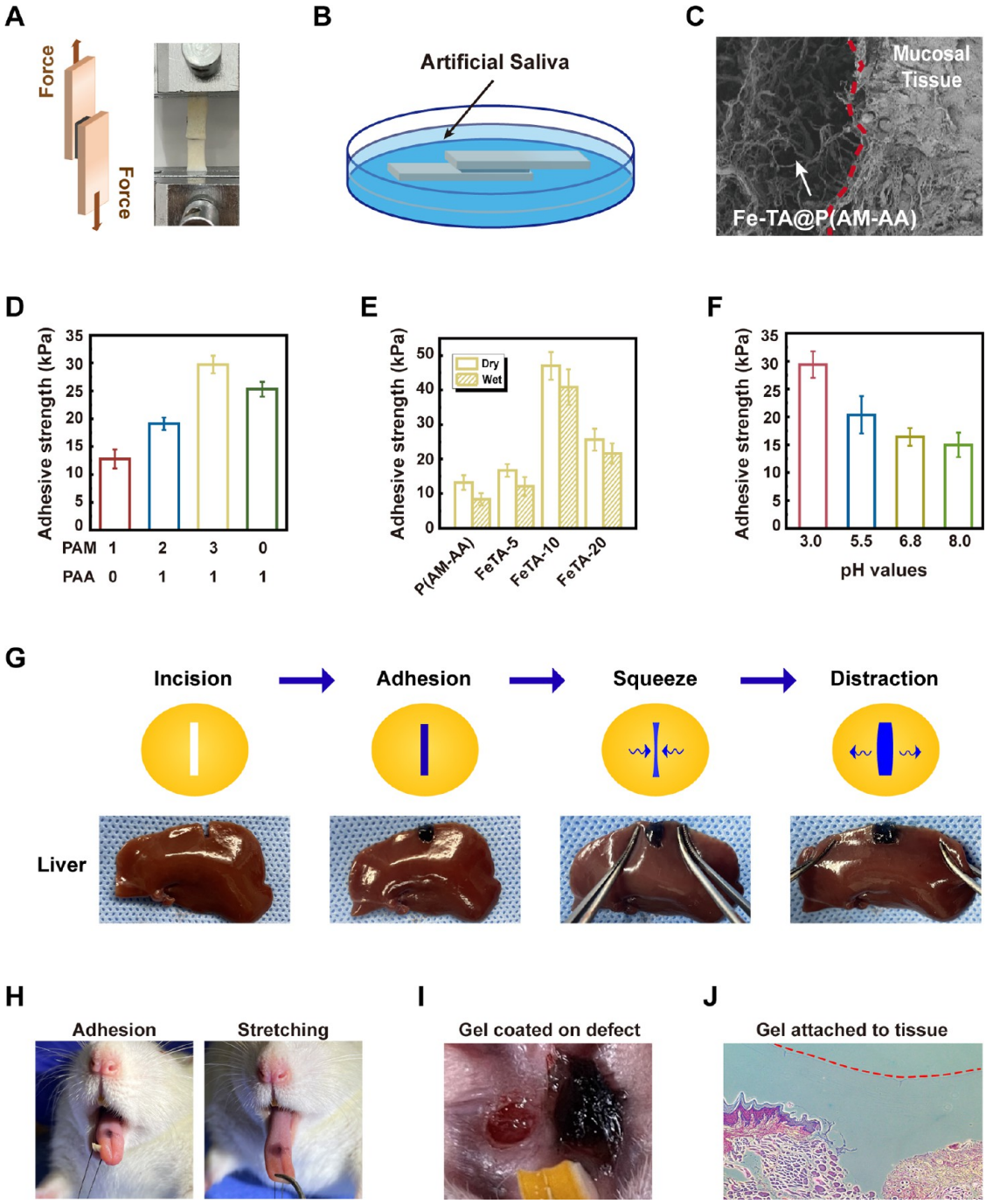

Figure 3. Adhesive performance of the Fe-TA@P(AM-AA) hydrogel. Models of porcine skin adhesive strength test via standard lap shear measurements in both (A) dry and (B) wet environments. (C) SEM observation of the integration of the Fe-TA@P(AM-AA) hydrogel with rat oral mucosal tissues (red dashed line indicates the boundary). (D) Adhesive strength of hydrogels with different ratios of PAM and PAA. (E) Adhesive strength of composite hydrogels under dry and wet conditions. (F) Adhesive strength of composite hydrogels soaked in artificial saliva with pH values of 3.0, 5.5, 6.8, and 8.0. (G) Images of the adhesiveness of the Fe-TA@P(AM-AA) hydrogel to the incisions on fresh rat liver. (H) Images of the superior adhesion and deformation of the Fe-TA@P(AM-AA) gel on the wet rat tongue along with tongue movement. (I) Images of the Fe-TA@P(AM-AA) gel applied in oral wound areas of diabetic rats. (J) Histological sections of rat oral mucosa, verifying the integration of the Fe-TA@P(AM-AA) gel with the mucosal epithelium.

(Figure 2C). Multiporous and interconnected microstructures of the prepared composite hydrogels were revealed by scanning electron microscopy (SEM) (Figure 2D), which were similar to the morphology of a regenerative extracellular matrix, capable of promoting cellular proliferation, angiogenesis, and nutrition transport,[27,28] thus accelerating wound repair. Further analysis of the pore size of hydrogels showed that pores of composite hydrogels containing Fe-TA displayed a smaller and much more well-distributed pattern (less than 30 μm), providing a suitable microenvironment for further adhesion and localization of cells.[29] The swelling property of Fe-TA@P(AM-AA) in PBS at 37 °C was subsequently investigated (Figure 2E). With an increase in the Fe^{3+} concentration, the maximum swelling ratio of the hydrogels

https://doi.org/10.1021/acsami.2c17424
ACS Appl. Mater. Interfaces 2023, 15, 416−431

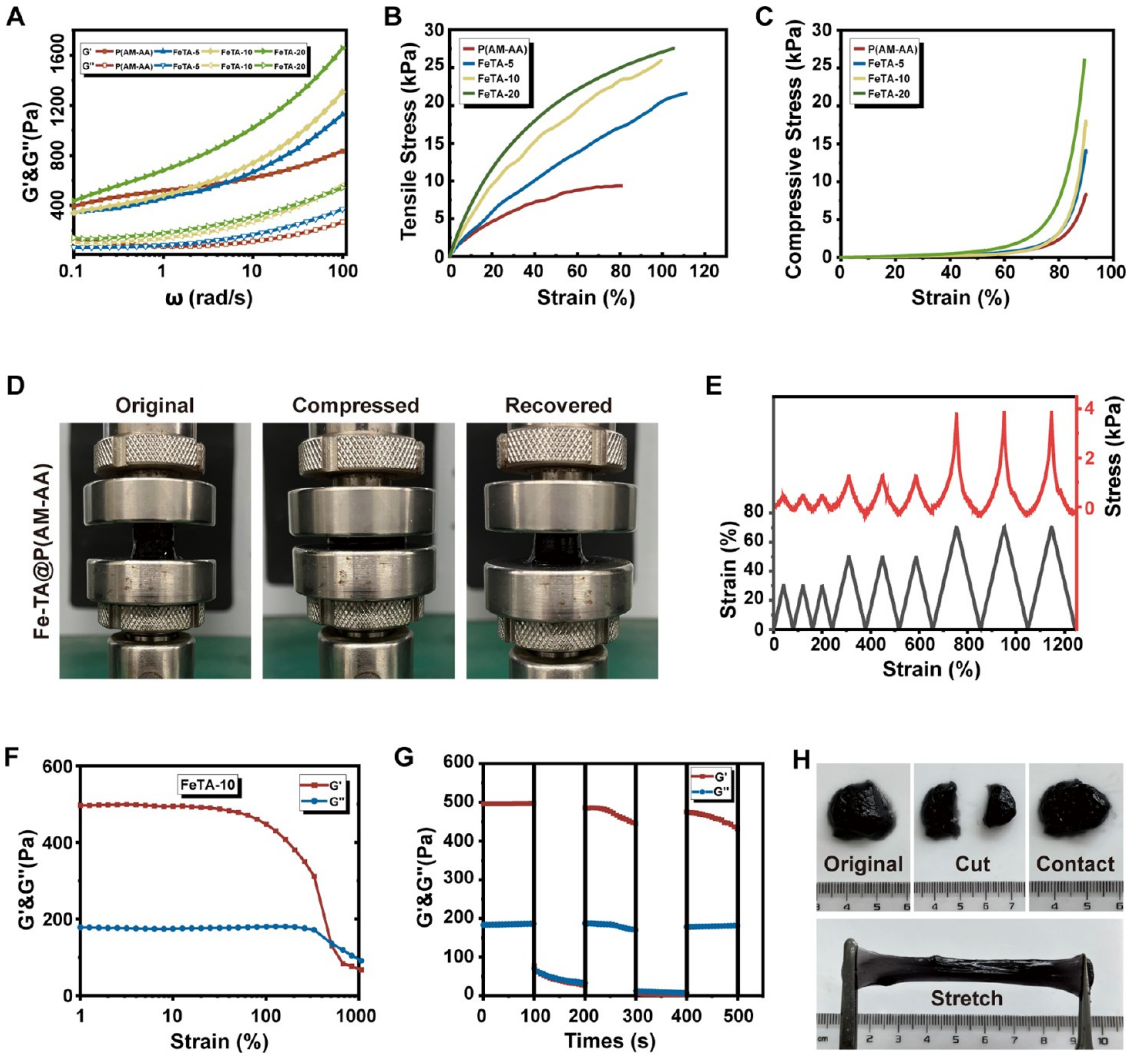

Figure 4. Mechanical properties of the Fe-TA@P(AM-AA) hydrogel. (A) Viscoelastic behavior of Fe-TA@P(AM-AA) hydrogels. (B) Tensile stress−strain curves of Fe-TA@P(AM-AA) hydrogels. (C) Compression stress−strain curves of Fe-TA@P(AM-AA) hydrogels. (D) Model of loading−unloading compression tests of Fe-TA@P(AM-AA) hydrogels. (E) Successive loading−unloading cycling compression tests of the Fe-TA@P(AM-AA) hydrogel, conducted three times at each of the strain ratios: 30, 50, and 70%. (F) Strain amplitude scan test of Fe-TA@P(AM-AA) hydrogels. (G) Continuous alternating strain scan of Fe-TA@P(AM-AA) hydrogels. (H) Images of self-healing properties of Fe-TA@P(AM-AA) hydrogels.

decreased from 402.1 ± 13.5 to 133.7 ± 4.2% (Figure 2F), which could be attributable to the changes in the crosslinking degree of hydrogels with different Fe^{3+} contents. Specifically, the crosslinking degree of the hydrogels improved with an increase in the Fe^{3+} content, leading to a tighter network structure of the hydrogels, and thus less space was left to store water. Notably, all hydrogels underwent the swell−shrink process, which could be explained by the electrostatic interaction between amino groups of the gels and phosphate in the buffer solution. After 5 days, the hydrogels reached swelling equilibrium, and the swelling ratios of both FeTA-10 and FeTA-20 were higher than 50%, which could maintain their gelation state and ensure long-term application in the oral environment to protect the wounded area from interference and accelerate the subsequent wound-healing process. Altogether, the above experiments verified the successful production of Fe-TA@P(AM-AA) hydrogels via the non-covalent crosslinking method, along with a biomimetic microstructure that is suitable for tissue regeneration.

Excellent Adhesive Performance of Fe-TA@P(AM-AA) Gels. To evaluate the adhesive performance of Fe-TA@P(AM-AA) in an oral environment and diabetic mode, we first adhered the hydrogels onto a porcine skin surface in both dry and wet environments (Figure 3A,B). Furthermore, SEM analysis further confirmed sufficient contact and firm adhesion between hydrogels and rat oral mucosal tissues (Figure 3C). In the shear lap test, the ratio of PAM and PAA at 3:1 exhibited the best performance of hydrogel adhesion (Figure 3D). As expected, despite the slight decrease in the wet adhesion ability on porcine skin as exhibited by all composite hydrogels when compared with that ubder dry conditions, FeTA-10 still presents the highest adhesion capability (Figure 3E), suggesting its superior adhesive potential in a wet oral environment, thus facilitating stable localization, protection of wound areas, and long-time exertion of biological effects from composite hydrogels.[30] When applied into incisive cracks created on liver, spleen, heart, and kidney samples, the Fe-TA@P(AM-AA) composite hydrogels could also act as sealing materials, which adhere tightly onto wet incisions and

https://doi.org/10.1021/acsami.2c17424
ACS Appl. Mater. Interfaces 2023, 15, 416−431

withstand external movements (Figures 3G and S3A), confirming their excellent wet adhesion on mucosal tissues. Increased levels of polyphenol groups from the addition of Fe-TA predominantly strengthened the interfacial adhesiveness and cohesion of hydrogels. This could mainly be explained by the strong binding affinity between polyphenol groups and thiol as well as amine groups from proteins on mucosal surfaces.[31,32] Chronic and nonhealing wounds are commonly observed in diabetic patients, which are described as being stuck in a persistent inflammatory status.[33] This prolonged inflammation contributed to the formation of a local environment with low pH value, unsuitable for adhesion and stabilization of current commercial oral adhesives.[34] Subsequently, considering the acidic microenvironment in wounded areas under diabetic conditions, a series of artificial saliva with a pH gradient was prepared to evaluate changes in adhesion in response to different acidities. Results exhibited that the wet adhesion of hydrogels significantly intensified along with decreasing environmental pH levels, confirming the strengthened adhesion potential of Fe-TA@P(AM-AA) in the acidic local environment caused by diabetes-induced local inflammation (Figure 3F). This could be attributed to the increased content of −COOH at the interface in an acidic environment, leading to strengthened hydrogen bonding and electrostatic interactions between −COOH in the hydrogel and $-NH_2$ on the tissue surface.[35] As a result of the excellent adhesion at lower pH values, the prepared hydrogels showed great potential for wound repair under diabetic conditions. Efforts were made to simulate the wet oral environment using different materials with artificial saliva at the same time, and results showed that strong binding between the composite hydrogel and different surfaces could be established consistently (Figure S3B). Furthermore, Fe-TA@P(AM-AA) was applied on the surface of rat tongues, and it was observed to adhere firmly while counteracting the repeated stretching and compression to avoid unnecessary displacement (Figures 3H and S4). Further, the addition of the composite hydrogels onto oral mucosal defects in diabetic rats still exhibited a rapid and tight adhesion (Figure 3I). Finally, frozen sections of samples collected upon Fe-TA@P(AM-AA) hydrogel treatment showed that defect regions were completely filled and covered, establishing a stable interaction with wounded tissues (Figure 3J). The remarkable underwater adhesion ability of mussel proteins attracted great attention for their potential application as excellent adhesives in a wet environment.[36] However, the predicament of isolation and purification restricted their broad popularization. Thus, mussel-inspired biomimetic adhesives, such as polydopamine-based hydrogels, have been applied in wet adhesion, including buccal and gastric mucosa.[25,37] Therefore, the outstanding adhesion performance of the prepared hydrogels endowed a strong adherence and blockade to diabetic wounded areas faced with low pH and a wet microenvironment, thus providing a suitable condition for tissue repair and regeneration.

Mechanical Properties of Fe-TA@P(AM-AA) Gels. Efforts were then made to detect the mechanical properties of hydrogels to resist possible damage caused by the flushing and flowing of oral contents. Increased concentrations of Fe-TA contributed to higher G' and G'', which was attributed to the enhancement of the crosslinking density in hydrogels (Figure 4A). Meanwhile, both the tensile and the compression strength showed an increasing tendency upon the addition of Fe-TA, which could be explained by the increased hydrogen bonds and electrostatic interactions (Figure 4B,C). Results of cyclic compression experiments further demonstrated the stability and fatigue resistance of Fe-TA@P(AM-AA) to sustain and adapt to the dynamic oral environment (Figures 4D,E and S1). In addition, the self-healing ability is vital for wound healing as it can effectively ensure wound closure and prevent wound infection. The strain amplitude scanning and continuous strain cyclic scanning of the composite hydrogel showed that the process of collapse and rearrangement of the gel network could be repeated several times at high (1000%) and low strains (10%), indicating that the prepared hydrogel possessed an excellent self-healing ability (Figure 4F,G). Subsequently, the composite hydrogel was cut into two pieces and placed adjacently; then, these two broken pieces of FeTA-10 hydrogel recovered into the initial shape within 5 min. The healed hydrogel can be stretched, further demonstrating its excellent self-healing property (Figure 4H). The test for viscoelasticity indicated the shear-thinning behavior of composite hydrogels (Figure S2A), and the gels could be easily syringed out to control their size and shape, also verifying the excellent injectability of composite hydrogels (Figure S2B). Single mussel-like biomaterials exhibited inadequate mechanical properties, including toughness, stiffness, and tensile strength, rendering them incapable of resisting bathing and flushing in the oral cavity. In addition, diabetes-induced prolonged inflammation forms an acidic local environment, which is unsuitable for stable adhesion and protection of oral wounds.[38] The significantly enhanced mechanical properties of the composite gel could facilitate long-term localization and stabilization of hydrogels in the oral cavity considering the complex and dynamic environment under constant food and fluid flushing, thus prolonging its application in oral wound healing. In summary, the above results demonstrated the superior stability, injectability, self-healing, and mechanical properties of Fe-TA@P(AM-AA) for its potential application in complex oral wound repair. Considering the excellent wet adhesion and mechanical properties of Fe-TA@P(AM-AA), it might also be applied as a sealant for protecting and curing wounds in other human organs, including gastric ulcers and liver incisions, due to its strong adhesion and stable attachment to human tissues.

Cytotoxicity and Biocompatibility of Fe-TA@P(AM-AA). The cytocompatibility of Fe-TA@P(AM-AA) was evaluated using oral epithelial cells. The cell counting kit-8 (CCK8) assay and live/dead cell staining results indicated no variations in cell viability after coculture with the extracts from composite hydrogels (Figure S5A,B). As expected, Fe-TA@P(AM-AA) did not affect cell apoptosis, further demonstrating its safety for cell survival (Figure S5C). In addition, macrophages showed favorable cell adhesion on different gels (Figure S6). Considering that the components of the gels are nature-derived without potential toxic substances and the noncovalent gelation process does not produce side effects, the composite gel would exert no adverse influence on biological safety.

Antioxidative and Immune-Modulating Roles of Fe-TA@P(AM-AA) in Diabetic Oral Wounds. To explore the antioxidative activity and immune modulation of Fe-TA@P(AM-AA) under diabetic conditions, we first evaluated its ability to resist oxidative stress under high-glucose conditions in vitro to simulate the strong oxidative stress in diabetic oral wounds. Compared with the high intensity of cellular reactive oxygen species (ROS) in the control group, Fe-TA@P(AM-

https://doi.org/10.1021/acsami.2c17424
ACS Appl. Mater. Interfaces 2023, 15, 416−431

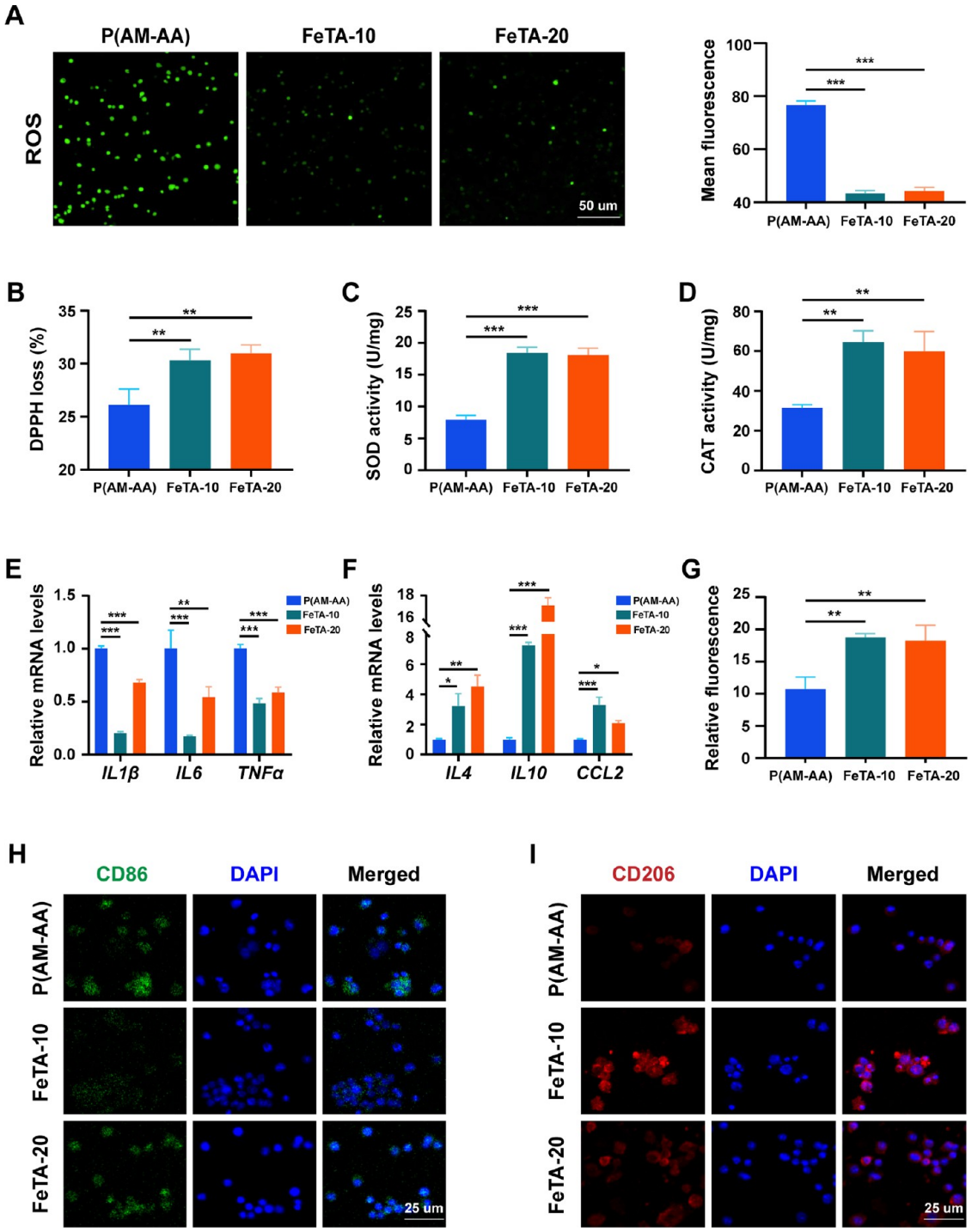

Figure 5. Fe-TA@P(AM-AA) exhibits obvious antioxidant capacity and improves the inflammatory microenvironment under high-glucose conditions in vitro. (A) Intracellular reactive oxygen species (ROS) production of macrophages cocultured with different hydrogel extracts for 48 h. (B) Free radical scavenging test for different composite hydrogels in vitro by incubation with DPPH for 30 min. (C) Intracellular superoxide dismutase (SOD) activity of macrophages cocultured with different hydrogel extracts for 48 h. (D) Intracellular catalase (CAT) activity of macrophages cocultured with different hydrogel extracts under high-glucose conditions for 48 h. (E, F) RT-qPCR analysis of the expression levels of M1 macrophage markers (IL1β, IL6, and TNFα) and M2 macrophage markers (IL4, IL10, and CCL2) in THP-1 cells cocultured with hydrogel extracts under high-glucose conditions for 48 h. (G) Percentage of CD206+ M2 macrophages measured by flow cytometry after coculturing with hydrogel extracts under high-glucose conditions for 48 h. (H, I) Immunofluorescence of macrophage M1 and M2 polarization status induced by hydrogel extracts under high-glucose conditions in vitro.

AA)-treated groups presented significantly decreased levels of ROS, confirming the capacity of the composite gels to eliminate excessive oxidative products (Figure 5A). To elucidate this phenomenon, the inherent ROS-eliminating efficiency was measured by a 2,2-di(4-*tert*-octylphenyl)-1-picrylhydrazyl (DPPH) clearing test. Fe-TA@P(AM-AA) exhibited a remarkable increase in free radical elimination compared with that in the control group, identifying its

https://doi.org/10.1021/acsami.2c17424
ACS Appl. Mater. Interfaces 2023, 15, 416−431

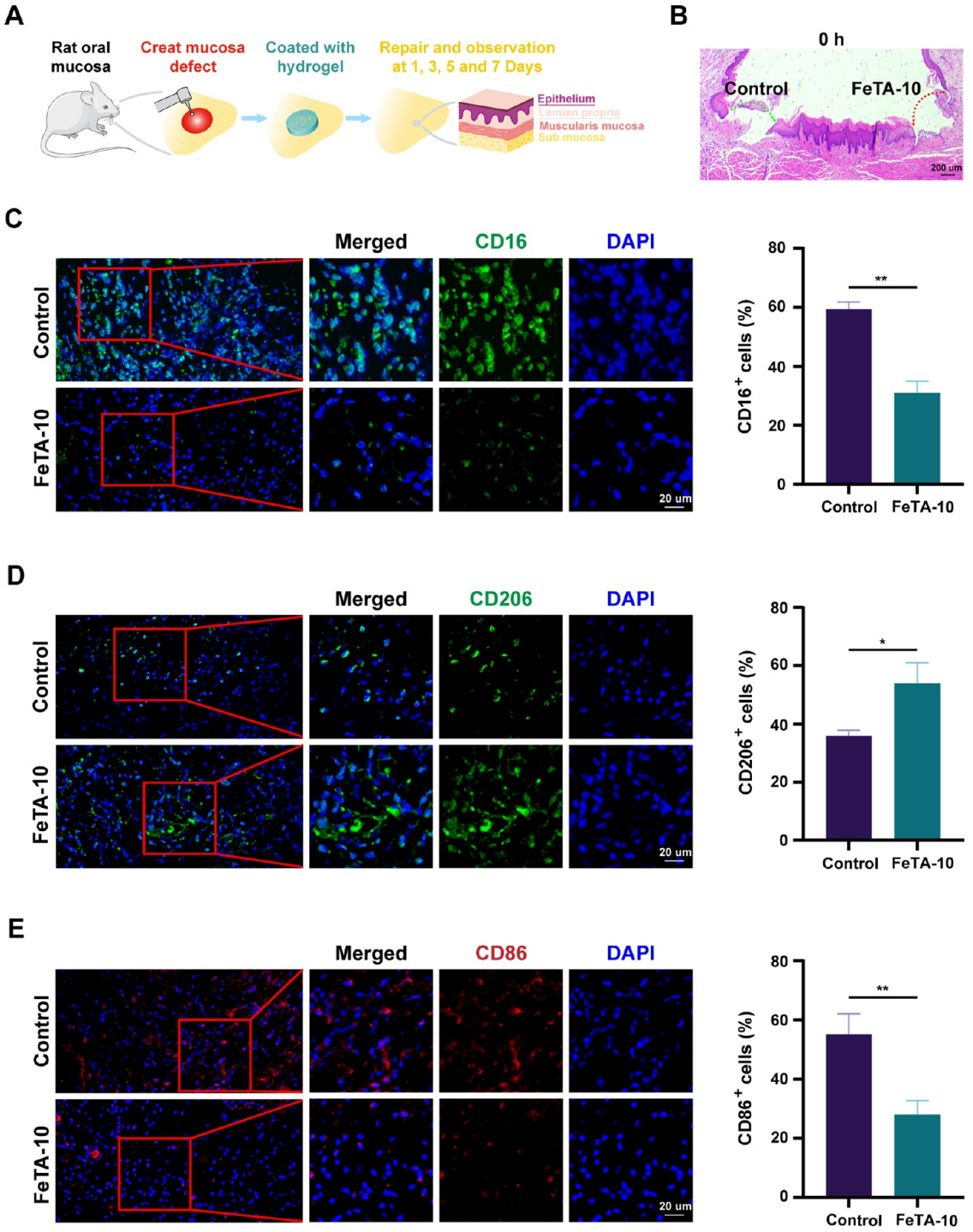

Figure 6. Fe-TA@P(AM-AA) improves the inflammatory microenvironment of diabetic oral wounds in vivo. (A) Scheme for the creation and covering of a diabetic rat palatal mucosal defect model to assess the wound-healing potential of gels. (B) H&E staining showing the successful creation of mucosal defects of the same size in the epithelium and lamina propria (labeled with dashed arrows) on both sides of the palatal mucosa. (C) CD16-stained neutrophils in the defect regions, with higher-magnification images of the regions marked by red boxes shown on the right. The percentage of CD16-positive cells was measured. (D) CD206-stained M2 macrophages in the defect regions, with higher-magnification images of the regions marked by red boxes shown on the right. The percentage of CD206-positive cells was measured. (E) CD86-stained M1 macrophages in the defect regions, with higher-magnification images of the regions marked by red boxes shown on the right. The percentage of CD86-positive cells was measured.

inherent activity in reacting with environmental ROS (Figure 5B). In addition, the treatment of composite gels also enhanced the cellular expression of superoxide dismutase (SOD) and catalase (CAT), both of which are well-acknowledged bioactive enzymes for ROS eradication, indicating its indirect effect on the promotion of the cellular antioxidative capacity (Figure 5C,D). Extreme oxidative stress induced by diabetes is a crucial reason for delayed wound healing, featured by the overproduction of ROS and subsequent biological disorders.[39] Thus, resisting local

https://doi.org/10.1021/acsami.2c17424
ACS Appl. Mater. Interfaces 2023, 15, 416−431

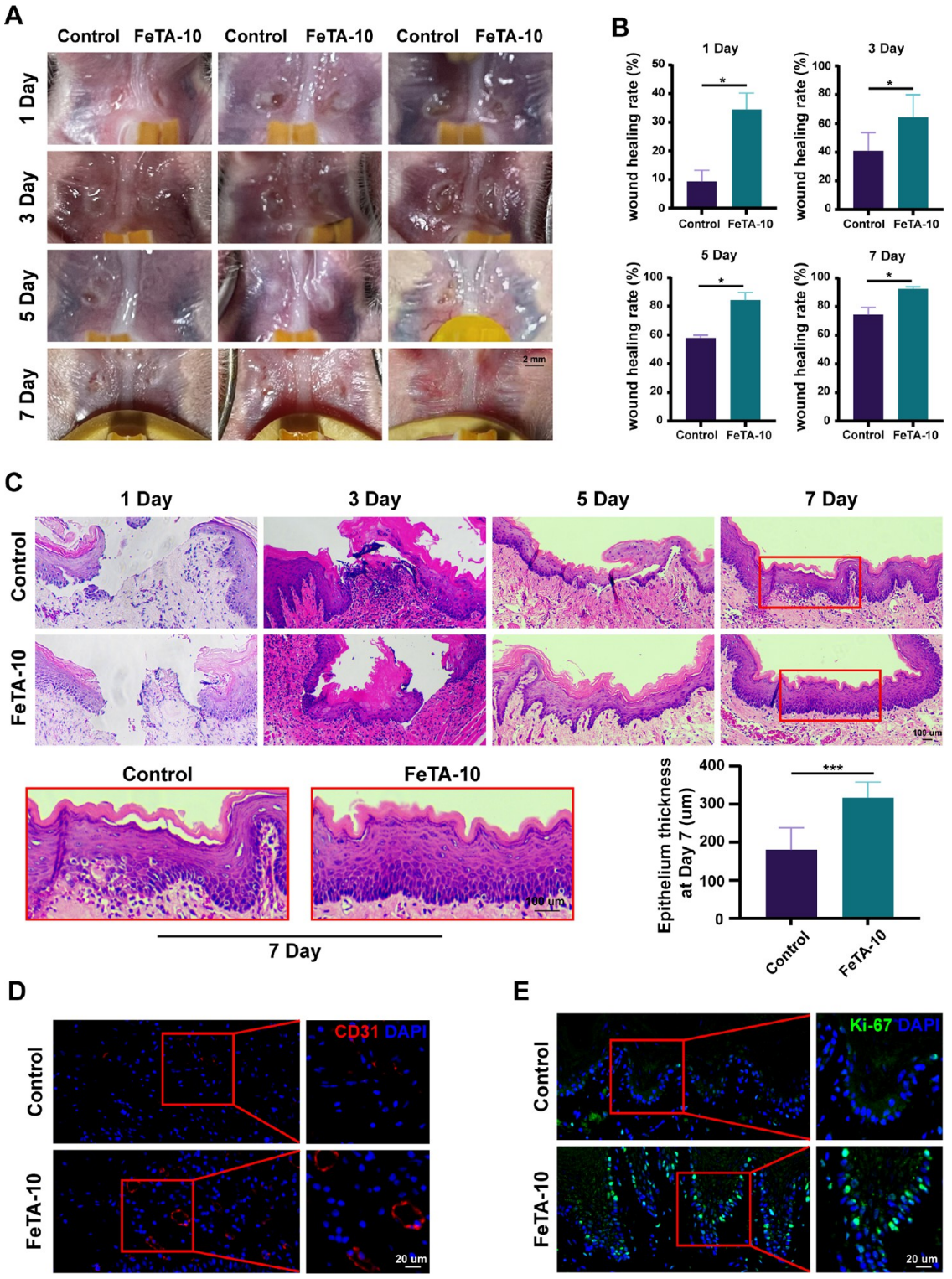

Figure 7. Fe-TA@P(AM-AA) promotes the wound healing of oral mucosa in the diabetic rat model. (A) Diabetic rat oral mucosa defects (1.2 mm diameter) were created above the muscle tissue and covered with Fe-TA@P(AM-AA) (10 wt %). Untreated oral mucosal defects were taken as the control group. (B) Wound-healing areas of rat oral mucosa were calculated on days 1, 3, 5, and 7 after treatment. (C) H&E staining showing the epithelial healing of the diabetic rat palatal mucosa defects at different time points. The thickness of the repaired epithelium was measured to evaluate the effect of the composite gel. (D) CD31-stained blood vessels in the defect regions. (E) Ki67-stained proliferative cells in the defect regions.

oxidative stress might be beneficial to rectify this functional abnormality. As expected, upon reversal of the environmental oxidative stress, the polarization status of macrophages was also transformed from the M1 inflammatory phenotype to the M2 repairing phenotype, as relative mRNA levels of IL1β, IL6, and TNFα were downregulated, while those of IL4, IL10, and CCL2 were all upregulated (Figure 5E,F), in combination with an enhanced percentage of CD206+ M2 macrophages

https://doi.org/10.1021/acsami.2c17424
ACS Appl. Mater. Interfaces 2023, 15, 416−431

measured by flow cytometry analysis (Figures 5G and S7A). In addition, Western blotting analysis also exhibited an increasing expression pattern of CD206 by Fe-TA@P(AM-AA) treatment (Figure S7B). Meanwhile, remarkably decreased levels of CD86 (M1 marker) and enhanced fluorescent intensity of CD206 (M2 marker) in Fe-TA@P(AM-AA)-treated macrophages were also observed (Figure 5H,I). Further, we created diabetic rat mucosal defects on the oral epithelial and lamina layers (Figures 6A,B and S8). By application of Fe-TA@P(AM-AA), fewer bacteria were detected in the wounded area (Figure S9). This could be explained by the physical barrier as well as chemical effects of released tannin for the inhibition of bacterial colonization and proliferation.[40] Subsequently, immunofluorescent staining also revealed fewer proinflammatory neutrophils (CD16 positive) accumulated in repaired regions of the Fe-TA@P(AM-AA) group (Figure 6C). In addition, a significant increase in M2 macrophages (CD206 positive) and decrease in M1 macrophages (CD86 positive) were observed in wounded areas (Figure 6D,E). The major mechanisms of pathogenesis of diabetic wounds are overall poorly controlled inflammatory responses featured by dysregulated neutrophil infiltration and proinflammatory macrophage polarization.[41] The suppression of oxidative stress discussed above might contribute to the immune regulatory effect of composite hydrogels in diabetic wounded areas. Based on the above results, it could be speculated that Fe-TA@P(AM-AA) facilitates the transformation of the immune microenvironment from a proinflammatory to a proregenerative status by directly and indirectly preventing excessive oxidative stress. Compared with normal conditions, diabetic oral wounds exhibited enhanced oxidative stress, the reversal of which could efficiently relieve abnormal inflammatory reactions. Traditional methods mainly focused on the exogenous addition of antioxidizing agents, including puerarin, celastrol, and lignin−Ag nanoparticles. However, their long-term effect remains elusive, and they might weaken the tightness and bonding of the whole system.[42−44] This biological function of the composite gel might contribute to the acceleration of the delayed healing process caused by global diabetes.

Promotion of the Oral Wound-Healing Process under Diabetic Conditions by Fe-TA@P(AM-AA). To measure the therapeutic effect of Fe-TA@P(AM-AA) for oral defect repair, we performed constant surveillance of the wound-healing status post operation. With excellent adherence and protection of the gel, the unhealing areas in the Fe-TA@P(AM-AA)-treated group became much smaller compared with those in the control group (Figure 7A). Statistical analysis of healing rates further confirmed the accelerated healing efficiency of wounds in the Fe-TA@P(AM-AA) group (Figure 7B). One day post operation, the wound-healing rate reached 35% in the Fe-TA@P(AM-AA) group, which was predominantly higher than that in the control group. On day 7 after the operation, the mucosal defects showed an almost complete recovery in the Fe-TA@P(AM-AA) group. After repairing the defects with composite gels, fresh samples were collected for further experiments. Histological sections showed that wounded areas in the Fe-TA@P(AM-AA) group were almost covered with a newly regenerated epithelial layer (Figure 7C), while the untreated group exhibited a significant delay in tissue regeneration (lower thickness of the new epithelium), which was further characterized by the reduced number of CD31+ vessel structures and Ki-67+ proliferative cells (Figure 7D,E). These results collectively emphasize the fact that Fe-TA@P(AM-AA) possessed excellent potential for repairing oral defects under diabetic conditions. Based on the superior multiporous structure and hydrophilicity of Fe-TA@P(AM-AA), anti-inflammatory agents, antibacterial agents, and other types of therapeutics might be loaded in the composite hydrogel and released controllably to further enhance its potential for accelerating oral wound healing, which deserves further exploration.

CONCLUSIONS

In this study, a novel Fe-TA@P(AM-AA) adhesive was prepared via a noncovalent crosslinking reaction to overcome difficulties in the treatment of oral mucosal defects along with diabetes. The composite gel could adhere tightly onto wet oral mucosa and remain stable for a relatively long-term protection of the wounded area. Furthermore, Fe-TA@P(AM-AA) served as a superior antioxidative reagent that led to a reversal of diabetes-induced local oxidative stress and remodeling of the microenvironment by the induction of M2 macrophage polarization and reduction of neutrophil infiltration. These could altogether contribute to an accelerated wound-healing and tissue regeneration process. By the integration of multiple functions by simple components and convenient steps, Fe-TA@P(AM-AA) accurately fulfills the requirements for diabetic oral wound healing. Our study casts light on the development of innovative treatments with enhanced adherence in a wet and acidic environment as well as antioxidative and immune-regulating capacities for diabetic oral mucosal wounds. Thus, in future studies, the composite patch might be used as a carrier to encapsulate therapeutic agents with antibacterial or antioxidative properties for better improvement of its medical effects.

ASSOCIATED CONTENT

Supporting Information

The Supporting Information is available free of charge at https://pubs.acs.org/doi/10.1021/acsami.2c17424.

Repeated compressive tests of the Fe-TA@ P(AM-AA) hydrogel three times at 30, 50, and 70% strain (Figure S1); injectability properties of the Fe-TA@ P(AM-AA) hydrogel (Figure S2); wet adhesion of Fe-TA@P(AM-AA) (Figure S3); image of Fe-TA@P(AM-AA) remaining adhered on the surface of the wet rat tongue after tongue movement (Figure S4); cytocompatibility of the Fe-TA@P(AM-AA) hydrogel (Figure S5); cell adhesion and spreading on composite hydrogels (Figure S6); immunomodulatory potential of composite hydrogels on macrophage polarization (Figure S7); oral mucosa defects above the muscle tissue with the same size (1.2 mm diameter) were created in the diabetic rat (Figure S8); antibacterial effect of Fe-TA@P(AM-AA) gel on rat oral mucosa defects were analyzed at different time points (Figure S9); primers and parameters used for the PCR analysis (Table S1) (PDF)

AUTHOR INFORMATION

Corresponding Authors

Yingying Chu − *School of Chemistry, Chemical Engineering and Life Sciences, Wuhan University of Technology, Wuhan 430070, China*; Email: y.chu@whut.edu.cn

https://doi.org/10.1021/acsami.2c17424
ACS Appl. Mater. Interfaces 2023, 15, 416−431

Lili Chen − *Department of Stomatology, Union Hospital, Tongji Medical College, Huazhong University of Science and Technology, Wuhan 430022, China; School of Stomatology, Tongji Medical College, Huazhong University of Science and Technology, Wuhan 430030, China; Hubei Province Key Laboratory of Oral and Maxillofacial Development and Regeneration, Wuhan 430022, China;* Email: chenlili1030@hust.edu.cn

Cheng Yang − *Department of Stomatology, Union Hospital, Tongji Medical College, Huazhong University of Science and Technology, Wuhan 430022, China; School of Stomatology, Tongji Medical College, Huazhong University of Science and Technology, Wuhan 430030, China; Hubei Province Key Laboratory of Oral and Maxillofacial Development and Regeneration, Wuhan 430022, China;* orcid.org/0000-0003-4331-5320; Email: yangc715@126.com

Authors

Jiwei Sun − *Department of Stomatology, Union Hospital, Tongji Medical College, Huazhong University of Science and Technology, Wuhan 430022, China; School of Stomatology, Tongji Medical College, Huazhong University of Science and Technology, Wuhan 430030, China; Hubei Province Key Laboratory of Oral and Maxillofacial Development and Regeneration, Wuhan 430022, China*

Tiantian Chen − *School of Resources and Environmental Engineering, Wuhan University of Technology, Wuhan 430070, China*

Baoying Zhao − *Department of Stomatology, Union Hospital, Tongji Medical College, Huazhong University of Science and Technology, Wuhan 430022, China; School of Stomatology, Tongji Medical College, Huazhong University of Science and Technology, Wuhan 430030, China; Hubei Province Key Laboratory of Oral and Maxillofacial Development and Regeneration, Wuhan 430022, China*

Wenjie Fan − *Department of Stomatology, Union Hospital, Tongji Medical College, Huazhong University of Science and Technology, Wuhan 430022, China; School of Stomatology, Tongji Medical College, Huazhong University of Science and Technology, Wuhan 430030, China; Hubei Province Key Laboratory of Oral and Maxillofacial Development and Regeneration, Wuhan 430022, China*

Yufeng Shen − *Department of Stomatology, Union Hospital, Tongji Medical College, Huazhong University of Science and Technology, Wuhan 430022, China; School of Stomatology, Tongji Medical College, Huazhong University of Science and Technology, Wuhan 430030, China; Hubei Province Key Laboratory of Oral and Maxillofacial Development and Regeneration, Wuhan 430022, China*

Haojie Wei − *School of Chemistry, Chemical Engineering and Life Sciences, Wuhan University of Technology, Wuhan 430070, China*

Man Zhang − *Department of Stomatology, Union Hospital, Tongji Medical College, Huazhong University of Science and Technology, Wuhan 430022, China; School of Stomatology, Tongji Medical College, Huazhong University of Science and Technology, Wuhan 430030, China; Hubei Province Key Laboratory of Oral and Maxillofacial Development and Regeneration, Wuhan 430022, China*

Wenhao Zheng − *Department of Stomatology, Union Hospital, Tongji Medical College, Huazhong University of Science and Technology, Wuhan 430022, China; School of Stomatology, Tongji Medical College, Huazhong University of Science and Technology, Wuhan 430030, China; Hubei Province Key Laboratory of Oral and Maxillofacial Development and Regeneration, Wuhan 430022, China*

Jinfeng Peng − *Department of Stomatology, Union Hospital, Tongji Medical College, Huazhong University of Science and Technology, Wuhan 430022, China; School of Stomatology, Tongji Medical College, Huazhong University of Science and Technology, Wuhan 430030, China; Hubei Province Key Laboratory of Oral and Maxillofacial Development and Regeneration, Wuhan 430022, China*

Jinyu Wang − *Department of Stomatology, Union Hospital, Tongji Medical College, Huazhong University of Science and Technology, Wuhan 430022, China; School of Stomatology, Tongji Medical College, Huazhong University of Science and Technology, Wuhan 430030, China; Hubei Province Key Laboratory of Oral and Maxillofacial Development and Regeneration, Wuhan 430022, China*

Yifan Wang − *Department of Stomatology, Union Hospital, Tongji Medical College, Huazhong University of Science and Technology, Wuhan 430022, China; School of Stomatology, Tongji Medical College, Huazhong University of Science and Technology, Wuhan 430030, China; Hubei Province Key Laboratory of Oral and Maxillofacial Development and Regeneration, Wuhan 430022, China;* orcid.org/0000-0002-2829-5985

Lihong Fan − *School of Chemistry, Chemical Engineering and Life Sciences, Wuhan University of Technology, Wuhan 430070, China*

Complete contact information is available at: https://pubs.acs.org/10.1021/acsami.2c17424

Author Contributions

#J.S., T.C., and B.Z. contributed equally to this study.

Notes

The authors declare no competing financial interest.

■ ACKNOWLEDGMENTS

This work was supported in part by grants from the National Key R&D Program of China (2021YFC2400400/04, to L.C.), the Key Project of Hubei Province (2020BCA072, to C.Y.), and the Opening Foundation of Key Laboratory of Oral Frontal Development and Regeneration (2021kqhm001, to Y.C.). The authors thank Dr. Ping Liu at the Optical Bioimaging Core Facility of WNLO-HUST for the support and helpful discussions during data acquisition.

■ REFERENCES

(1) Dudding, T.; Haworth, S.; Lind, P. A.; Sathirapongsasuti, J. F.; Tung, J. Y.; Mitchell, R.; Colodro-Conde, L.; Medland, S. E.; Gordon, S.; Elsworth, B.; Paternoster, L.; Franks, P. W.; Thomas, S. J.; Martin, N. G.; Timpson, N. J. Genome Wide Analysis for Mouth Ulcers Identifies Associations at Immune Regulatory Loci. *Nat. Commun.* **2019**, *10*, No. 1052.

(2) Petersen, P. E.; Bourgeois, D.; Ogawa, H.; Estupinan-Day, S.; Ndiaye, C. The Global Burden of Oral Diseases and Risks to Oral Health. *Bull. W. H. O.* **2005**, *83*, 661−669.

(3) Toma, A. I.; Fuller, J. M.; Willett, N. J.; Goudy, S. L. Oral Wound Healing Models and Emerging Regenerative Therapies. *Transl. Res.* **2021**, *236*, 17−34.

(4) Angelov, N.; Moutsopoulos, N.; Jeong, M. J.; Nares, S.; Ashcroft, G.; Wahl, S. M. Aberrant Mucosal Wound Repair in the Absence of Secretory Leukocyte Protease Inhibitor. *Thromb. Haemostasis* **2004**, *92*, 288−297.

(5) Sculean, A.; Gruber, R.; Bosshardt, D. D. Soft Tissue Wound Healing around Teeth and Dental Implants. *J. Clin. Periodontol.* **2014**, *41*, S6−22.
(6) Glim, J. E.; Beelen, R. H.; Niessen, F. B.; Everts, V.; Ulrich, M. M. The Number of Immune Cells is Lower in Healthy Oral Mucosa Compared to Skin and Does Not Increase after Scarring. *Arch. Oral Biol.* **2015**, *60*, 272−281.
(7) Brizeno, L. A. C.; Assreuy, A. M.; Alves, A. P.; Sousa, F. B.; Silva, P. G. d. B.; de Sousa, S. C.; Lascane, N. A.; Evangelista, J. S.; Mota, M. R. Delayed Healing of Oral Mucosa in a Diabetic Rat Model: Implication of TNF-α, IL-1β and FGF-2. *Life Sci.* **2016**, *155*, 36−47.
(8) Lan, C. C.; Liu, I. H.; Fang, A. H.; Wen, C. H.; Wu, C. S. Hyperglycaemic Conditions Decrease Cultured Keratinocyte Mobility: Implications for Impaired Wound Healing in Patients with Diabetes. *Br. J. Dermatol.* **2008**, *159*, 1103−1115.
(9) Brownlee, M. Biochemistry and Molecular Cell Biology of Diabetic Complications. *Nature* **2001**, *414*, 813−820.
(10) Yuan, T.; Yang, T.; Chen, H.; Fu, D.; Hu, Y.; Wang, J.; Yuan, Q.; Yu, H.; Xu, W.; Xie, X. New Insights into Oxidative Stress and Inflammation during Diabetes Mellitus-accelerated Atherosclerosis. *Redox Biol.* **2019**, *20*, 247−260.
(11) Alzoubi, F.; Joseph, B.; Andersson, L. Healing of Soft Tissue Lacerations in Diabetic-induced Rats. *Dent. Traumatol.* **2017**, *33*, 438−443.
(12) Wang, Y.; Graves, D. T. Keratinocyte Function in Normal and Diabetic Wounds and Modulation by FOXO1. *J. Diabetes Res.* **2020**, *2020*, No. 3714704.
(13) Al-Mulla, F.; Leibovich, S. J.; Francis, I. M.; Bitar, M. S. Impaired TGF-β Signaling and a Defect in Resolution of Inflammation Contribute to Delayed Wound Healing in a Female Rat Model of Type 2 Diabetes. *Mol. BioSyst.* **2011**, *7*, 3006−3020.
(14) Serena, C.; Keiran, N.; Ceperuelo-Mallafre, V.; Ejarque, M.; Fradera, R.; Roche, K.; Nuñez-Roa, C.; Vendrell, J.; Fernández-Veledo, S. Obesity and Type 2 Diabetes Alters the Immune Properties of Human Adipose Derived Stem Cells. *Stem Cells* **2016**, *34*, 2559−2573.
(15) Amirrah, I. N.; Mohd Razip Wee, M. F.; Tabata, Y.; Bt Hj Idrus, R.; Nordin, A.; Fauzi, M. B. Antibacterial-Integrated Collagen Wound Dressing for Diabetes-Related Foot Ulcers: An Evidence-Based Review of Clinical Studies. *Polymers* **2020**, *12*, No. 2168.
(16) Lam, G.; et al. Hyperbaric Oxygen Therapy: Exploring the Clinical Evidence. *Adv. Skin Wound Care* **2017**, *30*, 181.
(17) Ye, S.; Jiang, L.; Wu, J.; Su, C.; Huang, C.; Liu, X.; Shao, W. Flexible Amoxicillin-Grafted Bacterial Cellulose Sponges for Wound Dressing: In Vitro and in Vivo Evaluation. *ACS Appl. Mater. Interfaces* **2018**, *10*, 5862−5870.
(18) Hong, J. P.; Jung, H. D.; Kim, Y. W. Recombinant Human Epidermal Growth Factor (EGF) to Enhance Healing for Diabetic Foot Ulcers. *Ann. Plast. Surg.* **2006**, *56*, 394−398. discussion 399−400.
(19) Galiano, R. D.; Tepper, O. M.; Pelo, C. R.; Bhatt, K. A.; Callaghan, M.; Bastidas, N.; Bunting, S.; Steinmetz, H. G.; Gurtner, G. C. Topical Vascular Endothelial Growth Factor Accelerates Diabetic Wound Healing through Increased Angiogenesis and by Mobilizing and Recruiting Bone Marrow-derived Cells. *Am. J. Pathol.* **2004**, *164*, 1935−1947.
(20) Xu, Z.; Han, S.; Gu, Z.; Wu, J. Advances and Impact of Antioxidant Hydrogel in Chronic Wound Healing. *Adv. Healthcare Mater.* **2020**, *9*, No. 1901502.
(21) Lamont, R. J.; Koo, H.; Hajishengallis, G. The Oral Microbiota: Dynamic Communities and Host Interactions. *Nat. Rev. Microbiol.* **2018**, *16*, 745−759.
(22) Hearnden, V.; Sankar, V.; Hull, K.; Juras, D. V.; Greenberg, M.; Kerr, A. R.; Lockhart, P. B.; Patton, L. L.; Porter, S.; Thornhill, M. H. New Developments and Opportunities in Oral Mucosal Drug Delivery for Local and Systemic Disease. *Adv. Drug Delivery Rev.* **2012**, *64*, 16−28.
(23) Fortelny, R. H.; Petter-Puchner, A. H.; Walder, N.; Mittermayr, R.; Ohlinger, W.; Heinze, A.; Redl, H. Cyanoacrylate Tissue Sealant Impairs Tissue Integration of Macroporous Mesh in Experimental Hernia Repair. *Surg. Endosc.* **2007**, *21*, 1781−1785.
(24) Yuk, H.; Varela, C. E.; Nabzdyk, C. S.; Mao, X.; Padera, R. F.; Roche, E. T.; Zhao, X. Dry Double-sided Tape for Adhesion of Wet Tissues and Devices. *Nature* **2019**, *575*, 169−174.
(25) Xu, X.; Xia, X.; Zhang, K.; Rai, A.; Li, Z.; Zhao, P.; Wei, K.; Zou, L.; Yang, B.; Wong, W. K.; Chiu, P. W.; Bian, L. Bioadhesive Hydrogels Demonstrating pH-independent and Ultrafast Gelation Promote Gastric Ulcer Healing in Pigs. *Sci. Transl. Med.* **2020**, *12*, No. eaba8014.
(26) Pan, W.; Qi, X.; Xiang, Y.; You, S.; Cai, E.; Gao, T.; Tong, X.; Hu, R.; Shen, J.; Deng, H. Facile Formation of Injectable Quaternized Chitosan/tannic Acid Hydrogels with Antibacterial and ROS Scavenging Capabilities for Diabetic Wound Healing. *Int. J. Biol. Macromol.* **2022**, *195*, 190−197.
(27) Xi Loh, E. Y.; Fauzi, M. B.; Ng, M. H.; Ng, P. Y.; Ng, S. F.; Ariffin, H.; Mohd Amin, M. C. I. Cellular and Molecular Interaction of Human Dermal Fibroblasts with Bacterial Nanocellulose Composite Hydrogel for Tissue Regeneration. *ACS Appl. Mater. Interfaces* **2018**, *10*, 39532−39543.
(28) Figueiredo, L.; Pace, R.; D'Arros, C.; Réthoré, G.; Guicheux, J.; Le Visage, C.; Weiss, P. Assessing Glucose and Oxygen Diffusion in Hydrogels for the Rational Design of 3D Stem Cell Scaffolds in Regenerative Medicine. *J. Tissue Eng. Regener. Med.* **2018**, *12*, 1238−1246.
(29) Cao, H.; Duan, L.; Zhang, Y.; Cao, J.; Zhang, K. Current Hydrogel Advances in Physicochemical and Biological Response-driven Biomedical Application Diversity. *Signal Transduction Targeted Ther.* **2021**, *6*, No. 426.
(30) Zhang, W.; Bao, B.; Jiang, F.; Zhang, Y.; Zhou, R.; Lu, Y.; Lin, S.; Lin, Q.; Jiang, X.; Zhu, L. Promoting Oral Mucosal Wound Healing with a Hydrogel Adhesive Based on a Phototriggered S-Nitrosylation Coupling Reaction. *Adv. Mater.* **2021**, *33*, No. 2105667.
(31) Guo, S.; Yao, M.; Zhang, D.; He, Y.; Chang, R.; Ren, Y.; Guan, F. One-Step Synthesis of Multifunctional Chitosan Hydrogel for Full-Thickness Wound Closure and Healing. *Adv. Healthcare Mater.* **2022**, *11*, No. 2101808.
(32) Guo, S.; Ren, Y.; Chang, R.; He, Y.; Zhang, D.; Guan, F.; Yao, M. Injectable Self-Healing Adhesive Chitosan Hydrogel with Antioxidative, Antibacterial, and Hemostatic Activities for Rapid Hemostasis and Skin Wound Healing. *ACS Appl. Mater. Interfaces* **2022**, *14*, 34455−34469.
(33) Salazar, J. J.; Ennis, W. J.; Koh, T. J. Diabetes Medications: Impact on Inflammation and Wound Healing. *J. Diabetes Its Complications* **2016**, *30*, 746−752.
(34) Latta, M. A.; Tsujimoto, A.; Takamizawa, T.; Barkmeier, W. W. Enamel and Dentin Bond Durability of Self-Adhesive Restorative Materials. *J. Adhes. Dent.* **2020**, *22*, 99−105.
(35) Fan, X.; Fang, Y.; Zhou, W.; Yan, L.; Xu, Y.; Zhu, H.; Liu, H. Mussel Foot Protein Inspired Tough Tissue-selective Underwater Adhesive Hydrogel. *Mater. Horiz.* **2021**, *8*, 997−1007.
(36) Mehdizadeh, M.; Weng, H.; Gyawali, D.; Tang, L.; Yang, J. Injectable Citrate-based Mussel-inspired Tissue Bioadhesives with High Wet Strength for Sutureless Wound Closure. *Biomaterials* **2012**, *33*, 7972−7983.
(37) Hu, S.; Pei, X.; Duan, L.; Zhu, Z.; Liu, Y.; Chen, J.; Chen, T.; Ji, P.; Wan, Q.; Wang, J. A Mussel-inspired Film for Adhesion to Wet Buccal Tissue and Efficient Buccal Drug Delivery. *Nat. Commun.* **2021**, *12*, No. 1689.
(38) Ikemura, K.; Kadoma, Y.; Endo, T. A Review of the Developments of Self-etching Primers and Adhesives -Effects of Acidic Adhesive Monomers and Polymerization Initiators on Bonding to Ground, Smear Layer-covered Teeth. *Dent. Mater. J.* **2011**, *30*, 769−789.
(39) Deng, L.; Du, C.; Song, P.; Chen, T.; Rui, S.; Armstrong, D. G.; Deng, W. The Role of Oxidative Stress and Antioxidants in Diabetic Wound Healing. *Oxid. Med. Cell. Longevity* **2021**, *2021*, No. 8852759.
(40) Widsten, P.; Cruz, C. D.; Fletcher, G. C.; Pajak, M. A.; McGhie, T. K. Tannins and Extracts of Fruit Byproducts: Antibacterial Activity

https://doi.org/10.1021/acsami.2c17424
ACS Appl. Mater. Interfaces 2023, 15, 416−431

Against Foodborne Bacteria and Antioxidant Capacity. *J. Agric. Food Chem.* **2014**, *62*, 11146−11156.
(41) Sawaya, A. P.; Stone, R. C.; Brooks, S. R.; Pastar, I.; Jozic, I.; Hasneen, K.; O'Neill, K.; Mehdizadeh, S.; Head, C. R.; Strbo, N.; Morasso, M. I.; Tomic-Canic, M. Deregulated Immune Cell Recruitment Orchestrated by FOXM1 Impairs Human Diabetic Wound Healing. *Nat. Commun.* **2020**, *11*, No. 4678.
(42) Jeon, Y. D.; Lee, J. H.; Lee, Y. M.; Kim, D. K. Puerarin Inhibits Inflammation and Oxidative Stress in Dextran Sulfate Sodium-induced Colitis Mice Model. *Biomed. Pharmacother.* **2020**, *124*, No. 109847.
(43) Zhang, C.; Zhao, M.; Wang, B.; Su, Z.; Guo, B.; Qin, L.; Zhang, W.; Zheng, R. The Nrf2-NLRP3-caspase-1 Axis Mediates the Neuroprotective Effects of Celastrol in Parkinson's Disease. *Redox Biol.* **2021**, *47*, No. 102134.
(44) Yang, W.; Xu, F.; Ma, X.; Guo, J.; Li, C.; Shen, S.; Puglia, D.; Chen, J.; Xu, P.; Kenny, J.; Ma, P. Highly-toughened PVA/nanocellulose Hydrogels with Anti-oxidative and Antibacterial Properties Triggered by Lignin-Ag Nanoparticles. *Mater. Sci. Eng., C* **2021**, *129*, No. 112385.

https://doi.org/10.1021/acsami.2c17424
ACS Appl. Mater. Interfaces 2023, 15, 416−431